Vector Magnetometry Using Silicon Vacancies in 4*H*-SiC Under Ambient Conditions

Matthias Niethammer,[1] Matthias Widmann,[1] Sang-Yun Lee,[1,*] Pontus Stenberg,[2] Olof Kordina,[2] Takeshi Ohshima,[3] Nguyen Tien Son,[2] Erik Janzén,[2] and Jörg Wrachtrup[1,4]

[1]*3rd Institute of Physics, University of Stuttgart, Pfaffenwaldring 57, 70569 Stuttgart, Germany*
[2]*Department of Physics, Chemistry and Biology, Linköping University, SE-58183 Linköping, Sweden*
[3]*National Institutes for Quantum and Radiological Science and Technology, Takasaki, Gunma 370-1292, Japan*
[4]*Max Planck Institute for Solid State Research, Heisenbergstraße 1, 70569 Stuttgart, Germany*

(Received 23 May 2016; revised manuscript received 19 July 2016; published 8 September 2016)

Point defects in solids promise precise measurements of various quantities. Especially magnetic field sensing using the spin of point defects has been of great interest recently. When optical readout of spin states is used, point defects achieve optical magnetic imaging with high spatial resolution at ambient conditions. Here, we demonstrate that genuine optical vector magnetometry can be realized using the silicon vacancy in SiC, which has an uncommon $S = 3/2$ spin. To this end, we develop and experimentally test sensing protocols based on a reference field approach combined with multifrequency spin excitation. Our work suggests that the silicon vacancy in an industry-friendly platform, SiC, has the potential for various magnetometry applications under ambient conditions.

DOI: 10.1103/PhysRevApplied.6.034001

I. INTRODUCTION

In the past decade, quantum magnetometry based on atomic scale defects such as the nitrogen-vacancy (NV) centers in diamond has attracted considerable interest since it can be utilized in various applications ranging from material to life sciences [1–6]. The NV high-spin system ($S = 1$) and its C_{3V} symmetry allow determining not only the field strength but also the polar-angle orientation of the external magnetic field [7,8]. The long-lived spin states and optically detected magnetic resonance (ODMR) have led to high sensitivity [1] and when combined with optical or scanning probe microscopy, optical magnetic imaging with nanometer-scale spatial resolution has been demonstrated as well [4,7,9–13].

Recently, silicon carbide (SiC) has been recognized as an emerging quantum material potentially offering a platform for room-temperature wafer-scale quantum technologies [14–21], benefiting from advanced fabrication [22–25]. Many intrinsic defects and their optical and spin-related properties vary depending on the polytype [26]. Among them, the divacancy and silicon vacancy (V_{Si}) in hexagonal and rhombic polytype SiC are known to have a spin angular momentum $S > 1/2$ [15,21,26–28]. It has been recently shown that their spins are controllable and optically detectable on a single spin level at both room [19] and cryogenic temperature [29] with a long spin-coherence time [19,29,30].

High-spin systems ($S > 1/2$) with a nonzero zero-field splitting (ZFS) in general allow for vector magnetometry because spin resonance transition frequencies depend on both strength and orientation of the applied magnetic field even when the Landé g factor is isotropic [7,31]. However, only partial orientation information can be extracted for spin systems with uniaxial symmetry, as spin transition frequencies do not show azimuthal dependence [7,31]. Therefore, one is limited to sense only inclination or amplitude [7,8,31,32]. Both the NV center in diamond and V_{Si} in hexagonal polytypes, e.g., 4*H*- and 6*H*-SiC, and a rhombic polytype, e.g., 15*R*-SiC, have the C_{3V} uniaxial symmetry, thus only allowing the detection of the polar angle of the applied field [7,8,31,32]. The four different NV orientations in diamond allow a full reconstruction of field vectors, but this method requires one to discriminate up to 24 possible orientations since one cannot find which transition belongs to which orientation [8]. In order to circumvent this problem, one must apply reference fields [8,10]. The C_{3V} symmetry and the single preferential spin orientation of the V_{Si} in SiC hinder genuine vector magnetometry since only the polar angle can be obtained [31,32]. However, the preferential alignment allows an unambiguous assignment of the observed resonance transitions while overlap of several resonance transitions from different NV orientations [33–35] adds complexity in experiments [36] and limits precision of sensing. This is a considerable advantage to cubic lattice systems such as diamond, where only complex growth can yield a similarly unique orientation [37–40]. Here, we demonstrate that although the V_{Si} in 4*H*-SiC exhibits only a unique spin orientation with uniaxial symmetry, all vector components of a magnetic field can also be reconstructed by combining reference fields with multifrequency spin excitation.

*s.lee@physik.uni-stuttgart.de

Furthermore, the ZFS of the V_{Si} in hexagonal polytypes of SiC exhibits a very weak temperature dependence [17]. These make the V_{Si} in SiC promising for magnetometry applications.

Below, we demonstrate how optical dc vector magnetometry can yield an unambiguous measurement of the vector components of a magnetic field using the V_{Si} in one of the hexagonal polytypes, 4*H*-SiC. We develop a simple model to explain transient spin excitation and the optical detection of spin signals. Their analysis provides a better understanding for the underlying optical cycle responsible for the ODMR of the V_{Si} in 4*H*-SiC.

II. ELECTRON SPIN RESONANCE OF SILICON VACANCY IN SILICON CARBIDE

The V_{Si} in 4*H*-SiC is a negatively charged spin-3/2 defect consisting of a vacancy on a silicon site which exhibits a C_{3v} symmetry [41], known as *V*2 or T_{V2} centers in the literature. The relevant spin Hamiltonian of the system [41,42], assuming uniaxial symmetry, is given as

$$H = hD[S_z^2 - S(S+1)/3] + g\mu_B \vec{B}_0 \cdot \vec{S}, \qquad (1)$$

where h is the Planck constant, g is the electron Landé g factor (2.004 [43]), μ_B is the Bohr magneton, and $\vec{B}_0$ describes the external magnetic field. Coupling to nuclear spins is ignored since ^{29}Si, the most abundant nuclear spin in SiC [28,44], is diluted in our sample [45]. D describes the axial component of spin dipole-dipole interaction. This is responsible for a splitting of ZFS $= 2D$ between $|M_S| = 3/2$ and $|M_S| = 1/2$ states at a zero magnetic field [31], as shown in Fig. 1(a). It has been suggested that optical excitation leads to spin polarization into the $M_S = \pm 1/2$ spin sublevels of the ground state due to spin-dependent intersystem crossing [19,32,46–49]. The fluorescence emission is brighter when the system is in one of the $M_S = \pm 3/2$ states which is the basis for optical detection of electron spin resonance [19,46]. Soykal *et al.* recently claimed the opposite: $M_S = \pm 3/2$ states are preferentially occupied and fluorescence emission is brighter when the $M_S = \pm 1/2$ and D is negative [49]. However, we will keep the former model for convenience as both two opposing models can explain the observed results.

The magnetic field dependence of the energy eigenvalues of each spin-quartet sublevel in the ground state is shown in Fig. 1(a). There is only a single transition at $f = 2D$ when no magnetic field is applied, where f is the resonance frequency. This degeneracy is lifted by an external magnetic field giving rise to multiple transitions. The number of observable transitions varies depending on the magnetic field orientation as shown in Figs. 1(b) and 1(c). f_{42} and f_{31}, corresponding to $M_S = +3/2 \leftrightarrow M_S = +1/2$ and $M_S = -1/2 \leftrightarrow M_S = -3/2$, respectively, for $|B_0| < D$ and $\theta = 0$, are most dominant and well observable in every orientation [31,32]. f_{21} is also an allowed transition between $M_S = +1/2$ and $M_S = -1/2$ at $\theta = 0$, and its strong transition probability is maintained for large θ. However, the optically induced polarization into $M_S = \pm 1/2$ states does not induce a population difference between these two states, thus its ODMR signal is not observable [16,19,43,50]. f_{41} and f_{32} are forbidden for $\theta = 0$ since they correspond to a $\Delta M_S = 2$ transition, but are easily detectable when $\theta \neq 0$ and $B_0 < 1$ mT [32]. These multiple transitions will be used to realize vector magnetometry as follows.

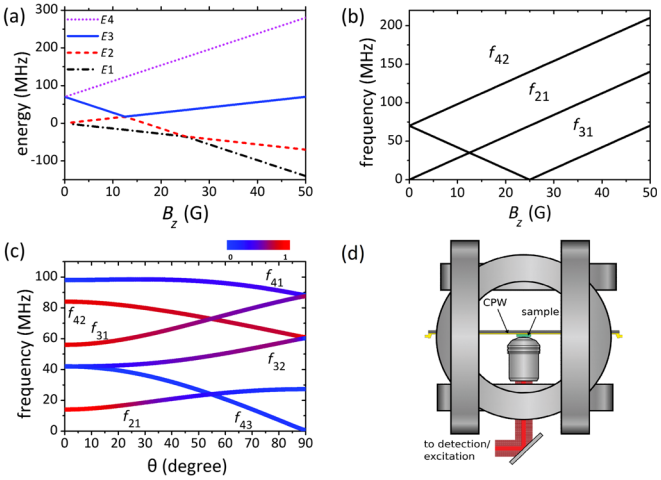

FIG. 1. (a) Magnetic field-strength dependence of the ground-state spin-quartet sublevels for V_{Si} in 4*H*-SiC with S = 3/2 when B_0 is aligned to the spin orientation. $2D = 70$ MHz is assumed. *E*1, *E*2, *E*3, and *E*4 states are sorted by energy eigenvalues in ascending order and correspond to $M_S = -1/2, +1/2, -3/2$, and $+3/2$ for $|B_0| < D$ and $M_S = -3/2, -1/2, +1/2$, and $+3/2$ for $|B_0| > 2D$. Energy is shown in frequency unit ($E = hf$). Expected (b) magnetic field dependence and (c) polar-angle dependence of the resonance transition frequencies of the ground-quartet state for the V_{Si} in 4*H*-SiC when $B_0 || c$ axis and $B_0 = 0.5$ mT, respectively. f_{ij} is the resonance frequency between Ei and Ej states. $f_{ij} = (Ei - Ej)/h$. The color scale indicates the calculated transition probability with B_1 perpendicular to the c axis. (d) A part of the experimental setup showing the SiC sample attached to a coplanar waveguide, which is used for rf irradiation, surrounded by three Helmholtz coil pairs. See Ref. [45] for the details of the experimental methods.

III. PRINCIPLE OF THE VECTOR MAGNETOMETRY

In general, spin-system magnetometery exploits the magnetic field dependence of spin resonance transition frequencies to reconstruct the magnetic field-vector components. This is often difficult, as an observed transition structure is not unique for an applied field [8]. Thus, reference fields, whose amplitude and orientation are known, are used to extract additional information [8,10]. Similar to the NV center in diamond [7], one can extract the applied field strength using a formula for the $S = 3/2$

quartet system when an unknown magnetic field vector is applied [31], for example,

$$B_0 = \left[\frac{h}{5g\mu_B}\{(\sqrt{3}f_{\mathrm{avg}} + f_{32})^2 - f_{42}f_{31} - 2(\sqrt{3}+1)f_{32}f_{\mathrm{avg}} - (2D)^2\}\right]^{1/2}, \quad (2)$$

where $f_{\mathrm{avg}} \equiv (f_{31} + f_{42})/2$ [see Fig. 1(c)]. Note that similar formulas utilizing other transitions, e.g., f_{41} instead of f_{32}, and a formula for $\cos^2\theta$ can also be found [31]. The formulas show that as long as one can find three resonance transitions, the applied magnetic field strength can be explicitly determined if the ZFS is known. In order to precisely determine the vector components of the unknown stray magnetic field, whose amplitude is

$$|\vec{B}_s| = \sqrt{B_{s,x}^2 + B_{s,y}^2 + B_{s,z}^2}, \quad (3)$$

three subsequent ODMR measurements with different reference fields should be performed. If the applied reference fields are perpendicular to each other, we obtain

$$|\vec{B}_s + \vec{B}_{\mathrm{ref},i}|^2 = (B_{s,i} + B_{\mathrm{ref},i})^2 + B_{s,j}^2 + B_{s,k}^2, \quad (4)$$

with $i, j, k \in \{(x, y, z)\}$. Using Eqs. (3) and (4),

$$B_{s,i} = \frac{|\vec{B}_s + \vec{B}_{\mathrm{ref},i}|^2 - |\vec{B}_s|^2 - B_{\mathrm{ref},i}^2}{2B_{\mathrm{ref},i}}. \quad (5)$$

Therefore, all the vector components of the unknown stray field $B_{s,i}$ can be obtained explicitly.

IV. METHODS AND MATERIALS

To demonstrate proof-of-principle experiments, we perform ODMR experiments without and with three reference fields (see Fig. 2). The sample used in the experiments is a 350-μm-thick ^{28}Si-enriched 4H-SiC layer grown on a natural 4H-SiC substrate in a horizontal hot-wall chemical-vapor-deposition system [45]. The sample is irradiated by 2-MeV electrons with a dose of 10^{16} cm^{-2} to create V_{Si} ensembles ($[V_{\mathrm{Si}}] \simeq 2 \times 10^{14}$ cm^{-3}) [45]. In the ODMR experiments, the sample is excited with a 785-nm laser focused by a lens. The fluorescence light from the sample is detected by a femtowatt Si photodiode or APDs after a 835-nm longpass filter. ODMR measurements are performed using a virtual lock-in for both continuous-wave and pulsed ODMR [45]. Reference fields are applied by three coil pairs in Helmholtz configuration [see Fig. 1(d)]. The ZFS of the V_{Si} in this sample is calibrated by measuring the maximum splitting between two allowed transitions, f_{42} and f_{31}, while applying $|B_0| \gg$ ZFS around the c axis [see Figs. 1(b) and 1(c)]. The obtained ZFS ($2D$) is 69.99 ± 0.03 MHz (data not shown). All measurements are performed at room temperature.

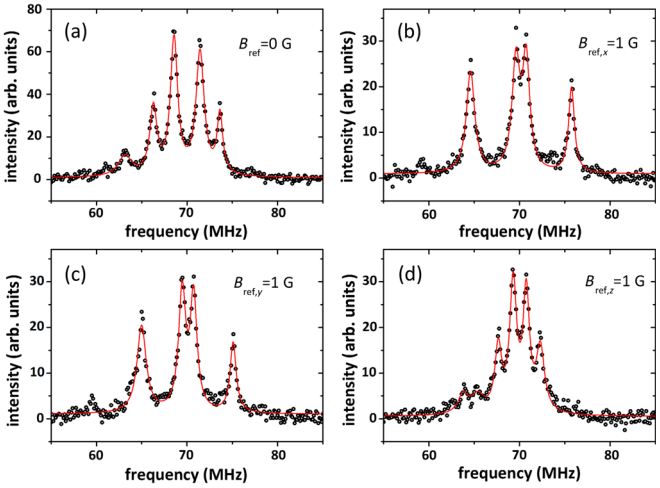

FIG. 2. ODMR spectra without and with reference fields. (a) ODMR spectrum without reference fields for which the stray magnetic field is to be determined. (b),(c), and (d) ODMR spectra with reference fields of $|B_0| = 0.1$ mT applied in x, y, and z directions, respectively. The red solid lines are the Lorentzian fit functions.

V. EXPERIMENTAL RESULTS

The measured continuous-wave ODMR spectra for a zero applied field and three reference fields of 0.1 mT are depicted in Fig. 2. One can identify four transitions corresponding to f_{41}, f_{42}, f_{31}, and f_{32} in all the observed spectra. It is, however, not possible to distinguish f_{42} and f_{31} using a single spectrum since their positions are interchanged at around the magic angle [see Fig. 1(c)] [31]. Accurate field measurements are, however, still possible because only f_{avg} and $f_{42}f_{31}$ are necessary to calculate the applied magnetic field strength as seen from Eq. (2). Note that additional peaks of unknown origin appear ~5 MHz below the f_{32} transition, which are under investigation and beyond the scope of this report. Since only a single transition should be observable in the absence of any stray magnetic field, the four transitions in Fig. 2(a) obtained without an applied magnetic field indicate a stray magnetic field in the experimental environment. Applying Eqs. (2) and (5) to these data, we obtain the stray magnetic field-vector components $B_{s,x} = 0 \pm 3$ μT, $B_{s,y} = -18 \pm 3$ μT, and $B_{s,x} = -60 \pm 2$ μT. These results are confirmed using a fluxgate sensor [45].

The presented method based on ODMR with continuous-wave spin excitation is simple and allows an accurate field-vector measurement. However, since at least three transitions need to be visible, this method is not applicable under certain conditions. f_{32} and f_{41} become hardly detectable for a small polar angle [31,32]. Therefore, it is necessary to find a way to detect an additional allowed

transition at f_{21}, which is usually not observable due to identical populations in $M_s = \pm 1/2$ [16,19,43,50]. One can create a population difference between these two states by applying a π pulse, swapping populations between $M_s = 3/2$ and $M_s = 1/2$ or $M_s = -1/2$ and $M_s = -3/2$ [50]. As will be seen below, because a single population swapping between these two states does not allow one to observe this hidden ODMR signal, we investigate a few pulse sequences based on multifrequency spin excitation and establish a rate model to explain how one can induce an optical contrast of spin signals.

The pulse sequences and resulting ODMR spectra under $B_0 = 0.543 \pm 0.003$ mT which is applied almost parallel to the spin sensor ($\theta = 3° \pm 1°$) are compared in Fig. 3. Note that these values for the magnetic field strength and orientation are extracted from Fig. 3(c) using Eq. (2) and Ref. [31]. These spectra exhibit additional side-peak structures because of excitation with a broadband rectangular rf pulse in contrast to the spectra in Fig. 2 which are measured with continuous-wave spin and optical excitation. When a rf pulse, whose frequency is being swept from 10 to 100 MHz (sweep pulse), is used, only two allowed transitions, f_{42} and f_{31}, are visible as shown in Fig. 3(a). Then, a π pulse between $M_S = 3/2$ and

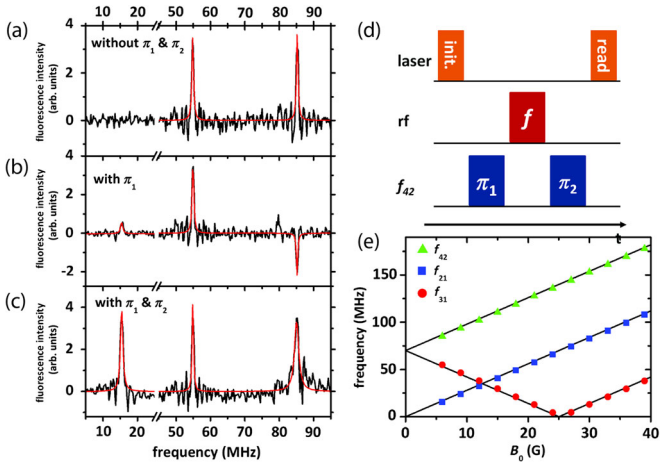

FIG. 3. Pulsed ODMR spectra at $B_0 = 0.543 \pm 0.003$ mT and $\theta = 3° \pm 1°$. ODMR with (a) only a sweep pulse, (b) an additional π pulse resonant to f_{42} before the sweep pulse, (c) two additional π pulses resonant to f_{42} before and after the sweep pulse. The red solid lines are the Lorentzian fit functions. (d) The used pulse sequences. A 600-ns-long laser pulse is for optical spin polarization as an initialization pulse. The same laser pulse is applied after the rf pulses for optical readout. A π pulse whose frequency (f) is being swept from 5 to 100 MHz is the sweep pulse. Two π pulses resonant to f_{42} (π_1 and π_2) are used for swapping the populations. The overall length of each sequence is approximately 4 μs. (e) Frequencies of the three resonant transitions including f_{21} obtained by the sequence used for (c) as a function of the applied magnetic field strength. The solid lines are the theoretical expectations. Error bars are smaller than the symbol size.

$M_S = 1/2$ corresponding to f_{42} is added before the sweep pulse in order to form a population difference between $M_S = \pm 1/2$ states. The missing transition f_{21} is, however, very weak, and we detect negative signals at f_{42} [Fig. 3(b)]. When the same π pulse is applied additionally after the sweep pulse, the f_{21} transition is clearly visible with the other two transitions as well [Fig. 3(c)]. In order to prove that this transition is from f_{21}, we monitor the magnetic field-strength dependence of the three transition frequencies measured by the pulse sequence with two π pulses at f_{42} as shown in Fig. 3(e). The position of the f_{21} transition is as expected from the spin Hamiltonian of Eq. (1) [19]. Since the detected signal sign is ambiguous in the lock-in experiment [51], we repeat these experiments without using lock-in methods and can confirm this result [45].

In order to explain the observed ODMR spectra in Fig. 3, we introduce a simplified model describing the ground-state population redistributed by the used pulse sequences as depicted in Fig. 4 [45]. We find that the change in the fluorescence intensity by swapping populations between two states is either zero or $(b-d)\Delta n_{g,0}$. Here, d and b are the rate-related parameters of $|M_S| = 1/2$ and $|M_S| = 3/2$, respectively, whose difference is determined by only the difference in the intersystem crossing rates, and $\Delta n_{g,0} \equiv n_{d,g,0} - n_{b,g,0}$, where $n_{d,g,0}$ and $n_{b,g,0}$ are the initial population of a $|M_S| = 1/2$ and $|M_S| = 3/2$ state, respectively. Since we assume that the $|M_S| = 1/2$ states are highly populated by optical polarization and fluorescence emission is brighter when $|M_S| = 3/2$ are highly occupied, $b > d$ and $\Delta n_{g,0} > 0$. See Ref. [45] for details. When a larger population is transferred to one of the $M_S = \pm 3/2$ states by the sweep pulse, one can see a fluorescence increase with respect to the off-resonance fluorescence intensity by

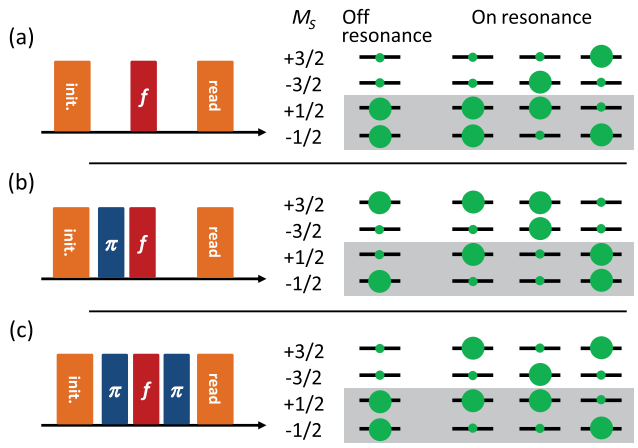

FIG. 4. Population redistribution by pulse sequences. Left column: pulse sequences used for the spectra in Figs. 3(a), 3(b), and 3(c), respectively. Right column: corresponding population distributions determined by each rf pulse sequence before the readout pulse. From left to right, when the sweep pulse is off resonant and resonant at f_{21}, f_{31}, and f_{42}, respectively.

$(b-d)\Delta n_{g,0}$, which is positive [see Fig. 4(a)]. This is consistent with the ODMR spectrum in Fig. 3(a). When the sweep pulse follows a π pulse at f_{42}, one, two, and none of the $M_S = \pm 3/2$ states are highly populated at resonances by the sweep pulse at f_{21}, f_{31}, and f_{42}, respectively [see Fig. 4(b)]. Since $M_S = 3/2$ is also highly populated when the sweep pulse is not resonant, zero, $(b-d)\Delta n_{g,0}$, and $-(b-d)\Delta n_{g,0}$ at these frequencies will be observed. This expectation is in agreement with what we experimentally observe as in Fig. 3(b). Therefore, additional population swapping by a π pulse at f_{42} following the resonant sweep pulses will allow us to have one of the $M_S = \pm 3/2$ states to be highly populated. In contrast, only the $M_S = \pm 1/2$ states will be highly populated at off resonance as depicted in Fig. 4(c), thus the same positive signals $(b-d)\Delta n_{g,0}$ at the three resonances will appear. This is exactly equivalent to our experimental observations in Fig. 3(c). This model can explain the signs and relative intensities of the observed ODMR signals well and detailed explanations can be found in Ref. [45]. We conclude that the presented sequence as in Fig. 4(c) allows us to observe the missing ODMR transition, and thus dc magnetometry becomes applicable for every orientation at the tested magnetic field strengths.

Though we aim to present proof-of-principle experiments for resolving an arbitrary magnetic field orientation, we provide discussions about the obtained sensitivity and its projection when the sample and detection methods are optimized. Note that if sensing only the magnetic field strength is of interest, phase-detection methods, e.g., the Ramsey interferometer, can be used instead which can enhance the sensitivity by many orders of magnitude [52]. The sensitivity extracted from the ODMR spectrum in Fig. 3(c) using Eq. (2) and the formula for $\cos^2\theta$ in Ref. [31] is 0.2 $\mathrm{mT}/\sqrt{\mathrm{Hz}}$ for the dc magnetic field strength and $30°/\sqrt{\mathrm{Hz}}$ for the orientation. The number of V_{Si} of the used sample within the focal volume is quite small ($\sim$2000) since the confocal microscope with a high NA objective is used [45]. If a larger V_{Si} concentration, e.g., $\sim 10^{16}$ cm^{-3} [48], is used, 30 $\mu\mathrm{T}/\sqrt{\mathrm{Hz}}$ and $7°/\sqrt{\mathrm{Hz}}$ can be expected with subwavelength spatial resolution. Substantial enhancement can be expected when high spatial resolution is not of interest; for example, up to 3 $\mathrm{nT}/\sqrt{\mathrm{Hz}}$ and $0.002°/\sqrt{\mathrm{Hz}}$ if $[V_{\mathrm{Si}}] \sim 10^{16}$ cm^{-3} in a 1-mm^3 volume device is used. These sensitivities can be even further enhanced if optimum detection methods are used. For example, a light-trapping waveguide and an optical cavity can improve the detection efficiency by many orders of magnitude [53,54]. A Hahn-echo sequence can be combined to the used sequence to improve the linewidth of the ODMR spectral lines. If a free precession time of 30 μs is used [19,55,56], since a linewidth of $\sim$10 kHz is expected, and the linewidth in Fig. 3 is $\sim$500 kHz, an order of magnitude higher sensitivity is expected considering the reduced duty cycle as well.

Now we discuss the dynamic range of the presented sensing methods. For small magnetic fields, e.g., $B_0 < hD/g\mu_B$, three transitions are necessary. Four transitions in Fig. 2 have been successfully observed up to 0.8 mT [32]. Thus, our methods are suitable for sub-mT dc vector magnetometry. When $B_0 \sim h2D/g\mu_B$, the suggested methods may not be useful because of complex spectra arising due to interactions among spin sublevels [56–58]. At high magnetic fields, e.g., $B_0 \sim 300$ mT, two transitions f_{21} and f_{43} are well observable at every orientation as experimentally reported [17,43]. The forbidden transitions are hardly visible in high magnetic field ranges. Therefore, it should be further investigated whether the missing transition between $M_S = \pm 1/2$, which is successfully observed with multifrequency excitation for the $B_0 \| c$ axis [50] can be well observed independent of the field orientation in this field range.

VI. SUMMARY

We demonstrate dc vector magnetometry based on the ODMR of $S = 3/2$ quartet spins of the V_{Si} in 4H-SiC at room temperature. ODMR scans with reference fields realize reconstruction of all vector components of the unknown magnetic field. We also demonstrate a pulse sequence based on multifrequency spin excitation as a complementary protocol to make this magnetometer practical. The suggested simple-rate model also provides a better understanding for the optical cycle allowing ODMR. With this sensing protocol, very weak temperature dependence of the ZFS [16] makes V_{Si} in SiC promising for robust magnetometer, and useful for optical magnetic imaging in nanoscale at ambient conditions. The possibility of electrically detected magnetic resonance [59–61] in the wafer scale SiC may also allow for the construction of an integrated quantum device for vector magnetometry.

ACKNOWLEDGMENTS

We acknowledge funding by the ERA.Net RUS Plus Program (DIABASE), the DFG via priority programme 1601, the EU via ERC Grant SQUTEC and Diadems, the Max Planck Society, the Knut and Alice Wallenberg Foundation, and KAKENHI (B) 26286047. We especially thank Corey Cochrane, Philipp Neumann, and Durga Dadari for inspiring discussions. We also thank Seoyoung Paik, Ilja Gerhardt, Florestan Ziem, Thomas Wolf, Amit Finkler, Roland Nagy, and Torsten Rendler for fruitful discussions.

[1] Romana Schirhagl, Kevin Chang, Michael Loretz, and Christian L Degen, Nitrogen-vacancy centers in diamond: Nanoscale sensors for physics and biology, Annu. Rev. Phys. Chem. **65**, 83 (2014).

[2] D. Le Sage, K. Arai, D. R. Glenn, S. J. DeVience, L. M. Pham, L. Rahn-Lee, M. D. Lukin, A. Yacoby, A. Komeili,

and R. L. Walsworth, Optical magnetic imaging of living cells, Nature (London) **496**, 486 (2013).

[3] L. P. McGuinness, Y. Yan, A. Stacey, D. A. Simpson, L. T. Hall, D. Maclaurin, S. Prawer, P. Mulvaney, J. Wrachtrup, and F. Caruso, Quantum measurement and orientation tracking of fluorescent nanodiamonds inside living cells, Nat. Nanotechnol. **6**, 358 (2011).

[4] L. T. Hall, D. A. Simpson, and L. C. L. Hollenberg, Nanoscale sensing and imaging in biology using the nitrogen-vacancy center in diamond, MRS Bull. **38**, 162 (2013).

[5] L. T. Hall, G. C. G. Beart, E. Thomas, D. A. Simpson, L. P. McGuinness, J. H. Cole, J. H. Manton, R. E. Scholten, F. Jelezko, J. Wrachtrup, S. Petrou, and L. C. L. Hollenberg, High spatial and temporal resolution wide-field imaging of neuron activity using quantum NV-diamond, Sci. Rep. **2**, 401 (2012).

[6] Liam T. Hall, Charles D. Hill, Jared H. Cole, Brigitte Städler, Frank Caruso, Paul Mulvaney, Jörg Wrachtrup, and Lloyd C. L. Hollenberg, Monitoring ion-channel function in real time through quantum decoherence, Proc. Natl. Acad. Sci. U.S.A. **107**, 18777 (2010).

[7] Gopalakrishnan Balasubramanian, I. Y. Chan, Roman Kolesov, Mohannad Al-Hmoud, Julia Tisler, Chang Shin, Changdong Kim, Aleksander Wojcik, Philip R Hemmer, Anke Krueger, Tobias Hanke, Alfred Leitenstorfer, Rudolf Bratschitsch, Fedor Jelezko, and Jorg Wrachtrup, Nanoscale imaging magnetometry with diamond spins under ambient conditions, Nature (London) **455**, 648 (2008).

[8] S. Steinert, High sensitivity magnetic imaging using an array of spins in diamond, Rev. Sci. Instrum. **81**, 043705 (2010).

[9] Christian Degen, Nanoscale magnetometry: Microscopy with single spins, Nat. Nanotechnol. **3**, 643 (2008).

[10] B. J. Maertz, A. P. Wijnheijmer, G. D. Fuchs, M. E. Nowakowski, and D. D. Awschalom, Vector magnetic field microscopy using nitrogen vacancy centers in diamond, Appl. Phys. Lett. **96**, 092504 (2010).

[11] Sungkun Hong, Michael S. Grinolds, Linh M. Pham, David Le Sage, Lan Luan, Ronald L. Walsworth, and Amir Yacoby, Nanoscale magnetometry with NV centers in diamond, MRS Bull. **38**, 155 (2013).

[12] M. S. Grinolds, M. Warner, K. De GreveK, Y. Dovzhenko, L. Thiel, R. L. Walsworth, S. Hong, P. Maletinsky, and A. Yacoby, Subnanometre resolution in three-dimensional magnetic resonance imaging of individual dark spins, Nat. Nanotechnol. **9**, 279 (2014).

[13] I. Jakobi, P. Neumann, Y. Wang, D. Dasari, F. El Hallak, M. A. Bashir, M. Markham, A. Edmonds, D. Twitchen, and J. Wrachtrup, Measuring nanoscale magnetic write head fields using a hybrid quantum register, arXiv:1602.02948.

[14] J. R. Weber, W. F. Koehl, J. B. Varley, A. Janotti, B. B. Buckley, C. G. Van de Walle, and D. D. Awschalom, Quantum computing with defects, Proc. Natl. Acad. Sci. U.S.A. **107**, 8513 (2010).

[15] William F. Koehl, Bob B. Buckley, F. Joseph Heremans, Greg Calusine, and David D. Awschalom, Room temperature coherent control of defect spin qubits in silicon carbide, Nature (London) **479**, 84 (2011).

[16] H. Kraus, V. A. Soltamov, D. Riedel, S. Vath, F. Fuchs, A. Sperlich, P. G. Baranov, V. Dyakonov, and G. V. Astakhov, Room-temperature quantum microwave emitters based on spin defects in silicon carbide, Nat. Phys. **10**, 157 (2014).

[17] H. Kraus, V. A. Soltamov, F. Fuchs, D. Simin, A. Sperlich, P. G. Baranov, G. V. Astakhov, and V. Dyakonov, Magnetic field and temperature sensing with atomic-scale spin defects in silicon carbide, Sci. Rep. **4**, 5303 (2014).

[18] A. Lohrmann, N. Iwamoto, Z. Bodrog, S. Castelletto, T. Ohshima, T. J. Karle, A. Gali, S. Prawer, J. C. McCallum, and B. C. Johnson, Single-photon emitting diode in silicon carbide, Nat. Commun. **6**, 7783 (2015).

[19] Matthias Widmann, Sang-Yun Lee, Torsten Rendler, Nguyen Tien Son, Helmut Fedder, Seoyoung Paik, Li-Ping Yang, Nan Zhao, Sen Yang, Ian Booker, Andrej Denisenko, Mohammad Jamali, S Ali Momenzadeh, Ilja Gerhardt, Takeshi Ohshima, Adam Gali, Erik Janzén, and Jörg Wrachtrup, Coherent control of single spins in silicon carbide at room temperature, Nat. Mater. **14**, 164 (2015).

[20] S. Castelletto, B. C. Johnson, V. Ivády, N. Stavrias, T. Umeda, A. Gali, and T. Ohshima, A silicon carbide room-temperature single-photon source, Nat. Mater. **13**, 151 (2014).

[21] V. A. Soltamov, B. V. Yavkin, D. O. Tolmachev, R. A. Babunts, A. G. Badalyan, V. Yu. Davydov, E. N. Mokhov, I. I. Proskuryakov, S. B. Orlinskii, and P. G. Baranov, Optically Addressable Silicon Vacancy-Related Spin Centers in Rhombic Silicon Carbide with High Breakdown Characteristics and ENDOR Evidence of Their Structure, Phys. Rev. Lett. **115**, 247602 (2015).

[22] Tsunenobu Kimoto and James A Cooper, *Fundamentals of Silicon Carbide Technology: Growth, Characterization, Devices and Applications* (John Wiley & Sons, Singapore, 2014).

[23] B Jayant Baliga, *Silicon Carbide Power Devices* (World Scientific, Singapore, 2005).

[24] Pasqualina M. Sarro, Silicon carbide as a new MEMS technology, Sens. Actuators A **82**, 210 (2000).

[25] N. G. Wright and A. B. Horsfall, SiC sensors: A review, J. Phys. D **40**, 6345 (2007).

[26] Abram L. Falk, Bob B. Buckley, Greg Calusine, William F. Koehl, Viatcheslav V. Dobrovitski, Alberto Politi, Christian A. Zorman, Philip X.-L. Feng, and David D. Awschalom, Polytype control of spin qubits in silicon carbide, Nat. Commun. **4**, 1819 (2013).

[27] T. Wimbauer, B. K. Meyer, A. Hofstaetter, A. Scharmann, and H. Overhof, Negatively charged Si vacancy in 4*H* SiC: A comparison between theory and experiment, Phys. Rev. B **56**, 7384 (1997).

[28] N. Mizuochi, S. Yamasaki, H. Takizawa, N. Morishita, T. Ohshima, H. Itoh, and J. Isoya, Continuous-wave and pulsed EPR study of the negatively charged silicon vacancy with $S = 3/2$ and C_{3v} symmetry in *n*-type 4*H*-SiC, Phys. Rev. B **66**, 235202 (2002).

[29] David J. Christle, Abram L. Falk, Paolo Andrich, Paul V. Klimov, Jawad Ul Hassan, Nguyen T. Son, Erik Janzén, Takeshi Ohshima, and David D. Awschalom, Isolated electron spins in silicon carbide with millisecond coherence times, Nat. Mater. **14**, 160 (2015).

[30] Li-Ping Yang, Christian Burk, Matthias Widmann, Sang-Yun Lee, Jörg Wrachtrup, and Nan Zhao, Electron spin

decoherence in silicon carbide nuclear spin bath, Phys. Rev. B **90**, 241203 (2014).
[31] Sang-Yun Lee, Matthias Niethammer, and Jörg Wrachtrup, Vector magnetometery based on $S = 3/2$ electronic spins, Phys. Rev. B **92**, 115201 (2015).
[32] D. Simin, F. Fuchs, H. Kraus, A. Sperlich, P. G. Baranov, G. V. Astakhov, and V. Dyakonov, High-Precision Angle-Resolved Magnetometry with Uniaxial Quantum Centers in Silicon Carbide, Phys. Rev. Applied **4**, 014009 (2015).
[33] Ngoc Diep Lai, Dingwei Zheng, Fedor Jelezko, François Treussart, and Jean-François Roch, Influence of a static magnetic field on the photoluminescence of an ensemble of nitrogen-vacancy color centers in a diamond single-crystal, Appl. Phys. Lett. **95**, 133101 (2009).
[34] Thiago P. Mayer Alegre, Charles Santori, Gilberto Medeiros-Ribeiro, and Raymond G. Beausoleil, Polarization-selective excitation of nitrogen vacancy centers in diamond, Phys. Rev. B **76**, 165205 (2007).
[35] Y. Matsuzaki, H. Morishita, T. Shimooka, T. Tashima, K. Kakuyanagi, K. Semba, W. J. Munro, H. Yamaguchi, N. Mizuochi, and S. Saito, Optically detected magnetic resonance of high-density ensemble of NV^- centers in diamond, J. Phys. Condens. Matter **28**, 275302 (2016).
[36] Alexander K. Dmitriev and Anton K. Vershovskii, Concept of a microscale vector magnetic field sensor based on nitrogen-vacancy centers in diamond, J. Opt. Soc. Am. B **33**, B1 (2016).
[37] Julia Michl, Tokuyuki Teraji, Sebastian Zaiser, Ingmar Jakobi, Gerald Waldherr, Florian Dolde, Philipp Neumann, Marcus W. Doherty, Neil B. Manson, Junichi Isoya, and Jörg Wrachtrup, Perfect alignment and preferential orientation of nitrogen-vacancy centers during chemical vapor deposition diamond growth on (111) surfaces, Appl. Phys. Lett. **104**, 102407 (2014).
[38] M. Lesik, J.-P. Tetienne, A. Tallaire, J. Achard, V. Mille, A. Gicquel, J.-F. Roch, and V. Jacques, Perfect preferential orientation of nitrogen-vacancy defects in a synthetic diamond sample, Appl. Phys. Lett. **104**, 113107 (2014).
[39] M. Lesik, T. Plays, A. Tallaire, J. Achard, O. Brinza, L. William, M. Chipaux, L. Toraille, T. Debuisschert, A. Gicquel, J. F. Roch, and V. Jacques, Preferential orientation of NV defects in CVD diamond films grown on (113)-oriented substrates, Diam. Relat. Mater. **56**, 47 (2015).
[40] L. M. Pham, N. Bar-Gill, D. Le Sage, C. Belthangady, A. Stacey, M. Markham, D. J. Twitchen, M. D. Lukin, and R. L. Walsworth, Enhanced metrology using preferential orientation of nitrogen-vacancy centers in diamond, Phys. Rev. B **86**, 121202 (2012).
[41] Erik Janzén, Adam Gali, Patrick Carlsson, Andreas Gällström, Björn Magnusson, and N. T. Son, The silicon vacancy in SiC, Physica (Amsterdam) **404B**, 4354 (2009).
[42] N. M. Atherton, *Ellis Horwood Series in Physical Chemistry* (Ellis Horwood, Chichester, 1993).
[43] E. Sörman, N. T. Son, W. M. Chen, O. Kordina, C. Hallin, and E. Janzén, Silicon vacancy related defect in 4*H* and 6*H* SiC, Phys. Rev. B **61**, 2613 (2000).
[44] N. Mizuochi, S. Yamasaki, H. Takizawa, N. Morishita, T. Ohshima, H. Itoh, and J. Isoya, EPR studies of the isolated negatively charged silicon vacancies in *n*-type 4*H*- and 6*H*-SiC: Identification of C_{3v} symmetry and silicon sites, Phys. Rev. B **68**, 165206 (2003).
[45] See Supplemental Material at http://link.aps.org/supplemental/10.1103/PhysRevApplied.6.034001 for details of the established rate model, materials and experimental methods, and additional data.
[46] Pavel G. Baranov, Anna P. Bundakova, Alexandra A. Soltamova, Sergei B. Orlinskii, Igor V. Borovykh, Rob Zondervan, Rogier Verberk, and Jan Schmidt, Silicon vacancy in SiC as a promising quantum system for single-defect and single-photon spectroscopy, Phys. Rev. B **83**, 125203 (2011).
[47] Victor A. Soltamov, Alexandra A. Soltamova, Pavel G. Baranov, and Ivan I. Proskuryakov, Room Temperature Coherent Spin Alignment of Silicon Vacancies in 4*H*- and 6*H*-SiC, Phys. Rev. Lett. **108**, 226402 (2012).
[48] F. Fuchs, B. Stender, M. Trupke, D. Simin, J. Pflaum, V. Dyakonov, and G. V. Astakhov, Engineering near-infrared single-photon emitters with optically active spins in ultrapure silicon carbide, Nat. Commun. **6**, 7578 (2015).
[49] Ö. O. Soykal, Pratibha Dev, and Sophia E. Economou, Silicon vacancy center in 4*H*-SiC: Electronic structure and spin-photon interfaces, Phys. Rev. B **93**, 081207 (2016).
[50] J. Isoya, T. Umeda, N. Mizuochi, N. T. Son, E. Janzén, and T. Ohshima, EPR identification of intrinsic defects in SiC, Physica Status Solidi (b) **245**, 1298 (2008).
[51] Sang-Yun Lee, Seoyoung Paik, Dane R. McCamey, and Christoph Boehme, Modulation frequency dependence of continuous-wave optically/electrically detected magnetic resonance, Phys. Rev. B **86**, 115204 (2012).
[52] C. L. Degen, Scanning magnetic field microscope with a diamond single-spin sensor, Appl. Phys. Lett. **92**, 243111 (2008).
[53] Hannah Clevenson, Matthew E. Trusheim, Carson Teale, Tim Schroder, Danielle Braje, and Dirk Englund, Broadband magnetometry and temperature sensing with a light-trapping diamond waveguide, Nat. Phys. **11**, 393 (2015).
[54] Y. Dumeige, M. Chipaux, V. Jacques, F. Treussart, J.-F. Roch, T. Debuisschert, V. M. Acosta, A. Jarmola, K. Jensen, P. Kehayias, and D. Budker, Magnetometry with nitrogen-vacancy ensembles in diamond based on infrared absorption in a doubly resonant optical cavity, Phys. Rev. B **87**, 155202 (2013).
[55] D. Simin, H. Kraus, A. Sperlich, T. Ohshima, G. V. Astakhov, and V. Dyakonov, Long-lived quantum memory in silicon carbide with natural isotope abundance, arXiv: 1602.05775.
[56] S. G. Carter, Ö. O. Soykal, Pratibha Dev, Sophia E. Economou, and E. R. Glaser, Spin coherence and echo modulation of the silicon vacancy in 4*H*-SiC at room temperature, Phys. Rev. B **92**, 161202(R) (2015).
[57] Xing-Fei He, Neil B. Manson, and Peter T. H. Fisk, Paramagnetic resonance of photoexcited *N-V* defects in diamond. I. Level anticrossing in the ^3A ground state, Phys. Rev. B **47**, 8809 (1993).
[58] D. Simin, V. A. Soltamov, A. V. Poshakinskiy, A. N. Anisimov, R. A. Babunts, D. O. Tolmachev, E. N. Mokhov, M. Trupke, S. A. Tarasenko, A Sperlich, P. G. Baranov, V. Dyakonov, and G. V. Astakhov, All-Optical dc Nanotesla Magnetometry Using Silicon Vacancy Fine Structure in

Isotopically Purified Silicon Carbide, Phys. Rev. X **6**, 031014 (2016).

[59] T. Umeda, R. Kosugi, K. Fukuda, N. Morishita, T. Oshima, K. Esaki, and J. Isoya, Electrically detected magnetic resonance (EDMR) studies of SiC-SiO_2 interfaces, Mater. Sci. Forum **717**, 427 (2012).

[60] C. J. Cochrane and P. M. Lenahan, Zero-field detection of spin dependent recombination with direct observation of electron nuclear hyperfine interactions in the absence of an oscillating electromagnetic field, J. Appl. Phys. **112**, 123714 (2012).

[61] E. Bourgeois, A. Jarmola, P. Siyushev, M. Gulka, J. Hruby, F. Jelezko, D. Budker, and M. Nesladek, Photoelectric detection of electron spin resonance of nitrogen-vacancy centres in diamond, Nat. Commun. **6**, 8577 (2015).